ELSEVIER

Biophysical Chemistry 50 (1994) 225–235

Biophysical Chemistry

Use of static and dynamic NMR microscopy to investigate the origins of contrast in images of biological tissues

Paul T. Callaghan [a,*], Christopher J. Clark [b], Lucy C. Forde [a]

[a] *Department of Physics and Biophysics, Massey University, Private Bag 11222, Palmerston North, New Zealand*
[b] *Horticulture and Food Research Institute of New Zealand, Ruakura Research Centre, Private Bag 3123, Hamilton, New Zealand*

(Received 5 January 1994)

Abstract

NMR imaging experiments have been carried out on a fruit (*Actinidia deliciosa*) and plant stem (*Stachys sylvatica*) using a wide range of image contrasts. These included T_1, T_2, T_2^*, diffusion, flow and chemical shift selection. In the case of fruit imaging we calculated relaxation time and diffusion maps and established that the imaged parameters varied significantly with fruit ripening. These changes we attribute to changes in water dynamics resulting from elevated sugar concentrations. For the plant stem, water flow has been observed in the xylem vessels with a maximum velocity of 70 $\mu m\ s^{-1}$. The role of image artifacts is considered and, in the case of transverse relaxation, we have demonstrated that it is necessary to use a precursor Carr–Purcell–Meiboom–Gill pulse train if additional diffusive attenuation is to be avoided.

Key words: *Actinidia deliciosa*; Biological tissue; Kiwifruit; Magnetic resonance imaging; NMR image contrast; *Stachys sylvatica*

1. Introduction

Nuclear magnetic resonance (NMR) microscopy is finding increasing acceptance as a non-destructive technology for investigating change in biological systems [1–4]. Because of their importance as a trade commodity, and their susceptibility to pathological and physiological disorders pre- and post-harvest, fruit have proved to be a popular subject for imaging [5–19]. In the majority of cases, the aim of these studies has been to employ the unique features of NMR imaging to describe anatomical features, or to make qualitative assessments of changes in image contrast during time-course experiments. Since the NMR signal intensity is affected by so many different factors [20], questions addressing the causes of image contrast have tended to be neglected or treated only superficially during studies of fruit. With advances in the type of pulse-sequence and image analysis techniques now available however [21–23], it is possible to attempt a more sophisticated interpretation by quantifying individually the effects which proton density, relaxation processes and diffusion contribute to image contrast. As an example of this approach we

* Corresponding author.

SSDI 0301-4622(94)00023-D

present the results of experiments in which a number of static and dynamic NMR imaging techniques were applied to analysis of ripening changes in a small fruit, and to measurement of flow in a stem tissue.

2. Theory

In nuclear magnetic resonance the precession of nuclear spins in the presence of a large polarizing magnetic field ($\boldsymbol{B}_0$) induces an oscillatory signal in a receiver coil placed around the sample, provided that those spins are initially disturbed from equilibrium by a resonant radiofrequency pulse. While a given 'species' of nuclear spins will have a common precession frequency (Larmor frequency, ω) in a given field, when these spins are located in a specific molecule differences in the local chemical environment of the nucleus give rise to subtle frequency variations known as the 'chemical shift'.

NMR imaging relies on the fact that the Larmor frequency is proportional to the local magnetic field. If in addition to the polarizing field, a magnetic field gradient ($\boldsymbol{G}$) is applied, then this frequency acquires a spatial signature. Provided that the frequency variations associated with this gradient are much larger than the chemical shift (or other delicate features of the NMR spectrum) then this dependence of frequency on position may be written

$$\omega(\boldsymbol{r}) = \gamma B_0 + \gamma \boldsymbol{G} \cdot \boldsymbol{r}, \qquad (1)$$

where γ is the nuclear gyromagnetic ratio. The simple linear relation between the Larmor frequency and the nuclear spin coordinates, $\boldsymbol{r}$, contains the essence of the imaging principle. Fig. 1a shows a simple pulse sequence involving the application of magnetic field gradients which allow a reconstruction of the nuclear spin density to be obtained. Since each isochromat of spins at position $\boldsymbol{r}$ precesses at local offset frequency $\gamma \boldsymbol{G} \cdot \boldsymbol{r}$, the net signal ($S$) in the heterodyne detection frame may be written [24]

$$S(\boldsymbol{k}) = \int \rho(\boldsymbol{r}) \exp(\mathrm{i}2\pi \boldsymbol{k} \cdot \boldsymbol{r})\, \mathrm{d}\boldsymbol{r}, \qquad (2)$$

where $\rho(\boldsymbol{r})$ is the nuclear spin density and $\boldsymbol{k}$ is the reciprocal space dimension conjugate to $\boldsymbol{r}$ and given by $(1/2\pi)\gamma \boldsymbol{G}t$, t being the evolution time. The NMR image is reconstructed by acquiring $S(\boldsymbol{k})$ over some appropriate volume of $\boldsymbol{k}$ space and performing an inverse Fourier transformation. Generally reconstruction is carried out in two dimensions using a plane of spins prepared by a frequency-selective excitation. This selection is usually carried out by employing a 'soft' (or narrow-band) rf pulse with an approximately rectangular frequency profile. Soft pulses have two main uses in imaging. When applied in the presence of a magnetic field gradient, they select a region of spins whose resonant frequencies lie within a desired slice oriented normal to the gradient axis. When applied in the absence of a magnetic field gradient, they can be used to excite spins lying in a specific region of the intrinsic NMR spectrum, a property which facilitates chemical selectivity.

Eqs. (1) and (2) represent a gross simplification since they ignore all interactions of the nuclear spins except those associated with the applied polarizing field and its gradient. While the additional interactions of nuclear spins with their molecular environment complicate this picture, they also provide a means by which additional contrast can be imparted to the imaging process. NMR imaging can provide unique, spatially resolved information about local diamagnetic susceptibility, chemical shift, dipolar, quadrupolar and scalar couplings, relaxation times and molecular translational motion. Providing that the inherent contrast is well understood, NMR imaging can also provide a direct measure of the numbers of resonant nuclei.

In the examples to be discussed in this article the contrast is deliberately applied prior to the acquisition of the signal under the read gradient. For example, the use of a chemical-shift selective pulse in the preparation period before signal acquisition dictates that $S(\boldsymbol{k})$ arises only from the spectral region of interest. Appropriate combinations of pulse delays cause the signal to be attenuated due to nuclear spin relaxation, while the use of motion-encoding gradient pulses can lead to signal attenuation or phase shifts arising from

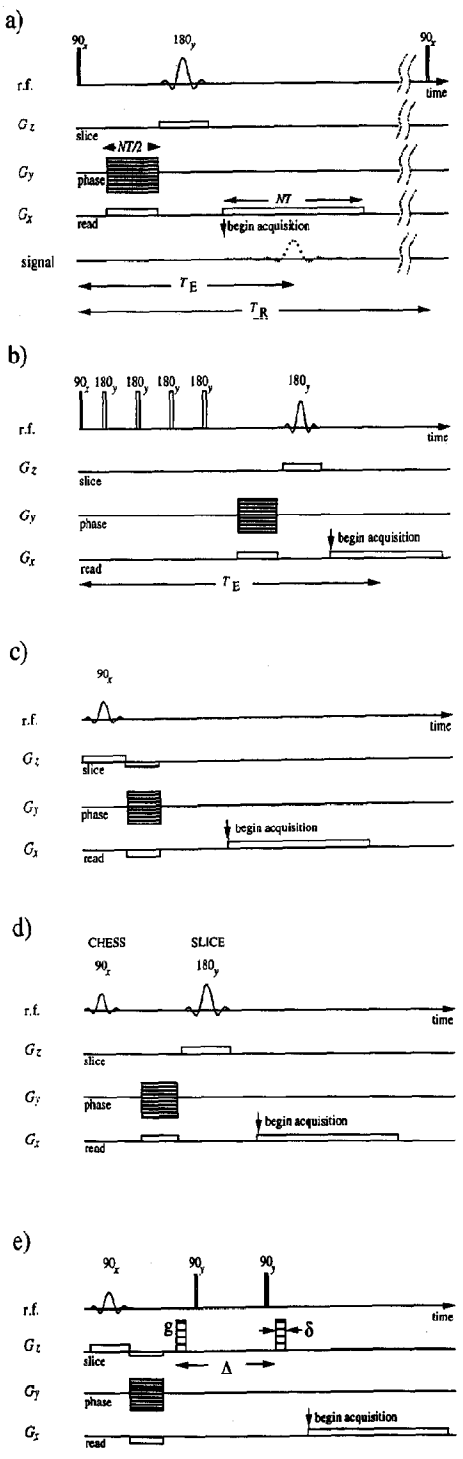

diffusion and flow respectively. These can be accounted for by incorporating a complex factor $C(\boldsymbol{r})$ in the integrand of Eq. (2).

The specific pulse sequences used in this work are all shown in Fig. 1. Fig. 1a illustrates the basic 'spin echo spin warp' sequence in which the refocussing 180° pulse is slice selective. The delay time, T_R, determines the degree to which the equilibrium magnetization is able to recover between pulse train repetitions while the delay time, T_E, determines the degree of transverse magnetization decay at the centre of $\boldsymbol{k}$ space. These delays therefore result in image sensitivity to T_1 and T_2 relaxation according to [22]

$$C(\boldsymbol{r}) = \{1 - \exp[-T_R/T_1(\boldsymbol{r})]\}\exp[-T_E/T_2(\boldsymbol{r})]. \quad (3)$$

It should be noted that the simple spin-echo sequence in Fig. 1a is sensitive to transverse relaxation effects caused by molecular diffusion in magnetic field gradients. Where T_E is sufficiently long that the rms molecular diffusion distance is comparable with a pixel dimension, the read gradient can be a cause of such additional T_2 relaxation. Alternatively strong local susceptibility variations may cause gradients sufficiently large to result in additional relaxation. We label the apparent T_2 values obtained using the spin-echo method as T_2-SE. One way to avoid such effects is to repetitively refocus the magnetization during the relaxation period T_E by employing a Carr–Purcell–Meiboom–Gill (CPMG) pulse train as shown in Fig. 1b. The relaxation times obtained in this way we term T_2-CPMG. The difference between T_2 maps obtained using the two pulse sequences of Figs. 1a and 1b can then be used to indicate the presence of diffusion-related relaxation.

One dramatic consequence of local variations in magnetic susceptibility is the inhomogeneous broadening of the NMR spectrum. This broaden-

Fig. 1. Pulse sequence diagrams for imaging experiments used in this work. (a) Standard spin-echo spin warp (T_1 and T_2-SE); (b) Carr–Purcell–Meiboom–Gill (T_2-CPMG); (c) gradient echo (T_2^*); (d) chemical shift selective imaging; (e) diffusion and flow contrast.

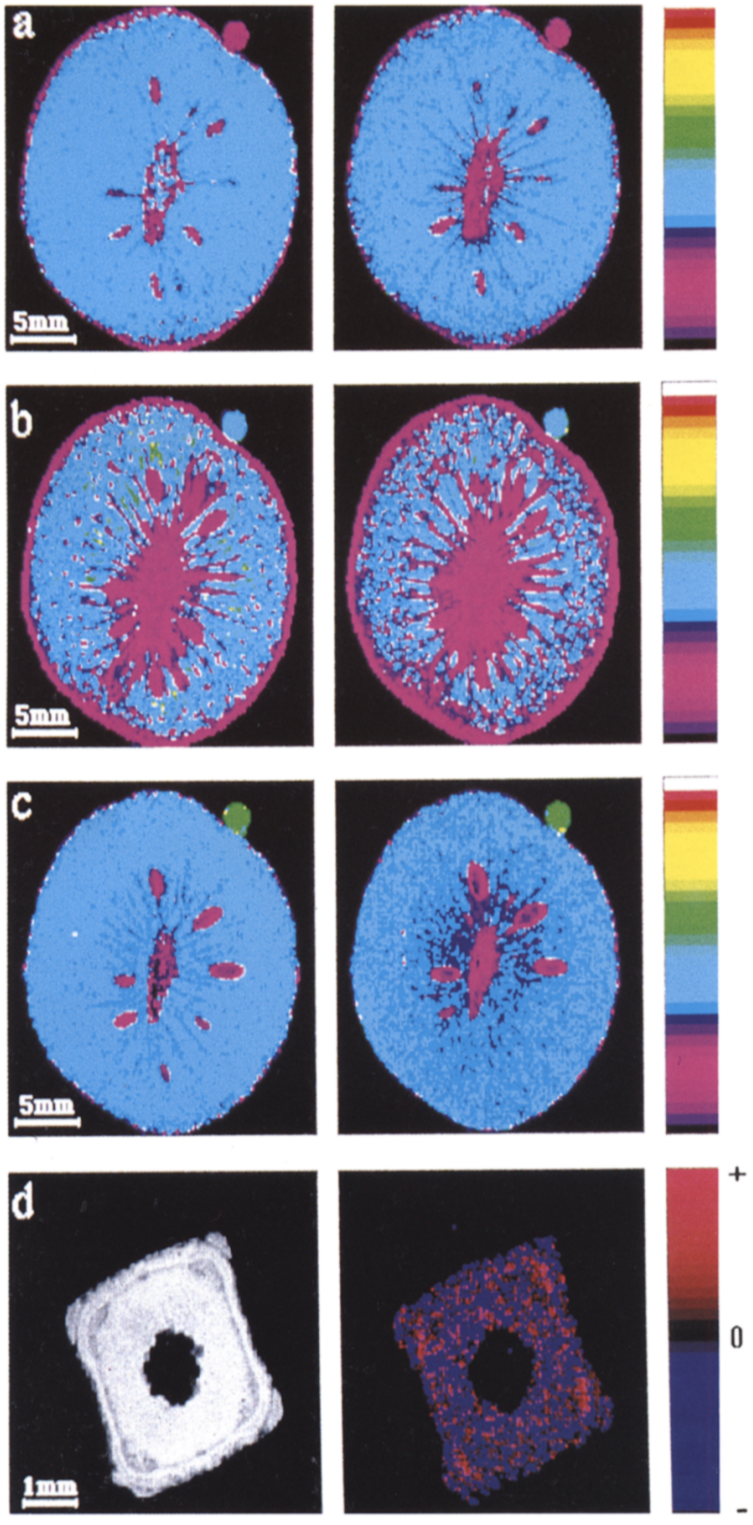
a
5mm
b
5mm
c
5mm
d
1mm
+
0
-

ing, arising from a distribution of local fields, causes dephasing of the magnetisation following excitation of the spins by the 90° rf pulse. This dephasing is refocused in a spin-echo sequence and is therefore invisible in images obtained using the pulse sequences of Figs. 1a and 1b. However, when a gradient- (rather than spin-) echo pulse train is employed (Fig. 1c), the spin dephasing leads to strong susceptibility contrast in which regions exhibiting the greatest local broadening suffer the greatest attenuation. The 'relaxation' contrast so obtained is known as T_2^*, and incorporates both the inhomogeneous broadening effect as well as the signal decay arising from true T_2 processes.

Fig. 1d shows an adaptation of the basic spin warp sequence depicted in Fig. 1a, as used for chemical shift selective imaging. Here a narrow band excitation pulse is centred on the region of the NMR spectrum corresponding to the desired molecule while the 180° refocussing pulse is used for slice selection.

The final image contrast discussed arises directly from molecular translational motion alone. Here a pair of gradient pulses of duration δ, separation Δ, and amplitude g (Fig. 1e), is used to impart a phase shift proportional to the distance, Z, moved by each molecule along the gradient direction over the time, Δ. This phase shift must then be averaged over the molecular ensemble, using a translational displacement probability distribution, $\overline{P}_s(Z, \Delta)$. Consequently Eq. (2) becomes

$$S(\boldsymbol{k}, q) = \int \rho(\boldsymbol{r}) \left(\int \overline{P}_s(Z, \Delta) \exp[i2\pi qZ] \, dZ \right) \times \exp(i\pi \boldsymbol{k} \cdot \boldsymbol{r}) \, d\boldsymbol{r}, \quad (4)$$

where q is $(2\pi)^{-1}\gamma g \delta$. Double inverse Fourier transformation of $S(\boldsymbol{k}, q)$ with respect to both $\boldsymbol{k}$ and q returns $\rho(\boldsymbol{r})\overline{P}_s(Z, \Delta)$. By normalising this function with the image density $\rho(\boldsymbol{r})$ acquired under zero PGSE gradient, one reconstructs $\overline{P}_s(Z, \Delta)$ for each pixel of the image. Conventionally the q gradient is stepped from zero to some maximum, typically in 16 steps. In that sense the method is akin to multi-slice imaging. For each step (or 'q slice') a complex image is reconstructed. At the completion of acquisition the modulated image signal for each pixel is Fourier transformed along the q direction to return $\overline{P}_s(Z, \Delta)$ thus enabling details of the local motion to be calculated. The width of $\overline{P}_s(Z, \Delta)$ is determined by the rms Brownian motion $(2D_s\Delta)^{1/2}$ and can therefore be used to construct a map of molecular self-diffusion coefficients, $D_s(\boldsymbol{r})$. Alternatively a map can be obtained directly by analysing the image attenuation as a function of increasing q. The displacement of $\overline{P}_s(Z, \Delta)$ along the Z axis is determined by the flow displacement $v\Delta$, where v is the local molecular velocity. In this manner a map of the local flow velocity, $v(\boldsymbol{r})$, may be constructed.

3. Materials and methods

3.1. Samples

Small self-fertile kiwifruit (*Actinidia deliciosa*, C.F. Liang and A.R. Ferguson var *deliciosa*) were sampled from a male vine in May 1993, coinciding with the timing of commercial harvest of the much larger fruit set on female vines which we wished to model: typically kiwifruit is dioecious although there are a few male selections which contain flowers that have a functioning ovary and set small fruit. For imaging, one fruit, approximately 22 mm in diameter, was positioned firmly in a pyrex glass tube along with moisture-soaked cotton wool (to prevent sample dehydration) and a reference capillary tube filled with 0.004 M $CuSO_4$. The pyrex sample holder was sealed and

Fig. 2. Calculated maps for kiwifruit of (a) T_1 relaxation times; (b) T_2-CPMG relaxation times; (c) molecular self-diffusion coefficients; (d) a standard proton spin echo image (left-hand panel) and velocity map (right-hand panel) for *Stachys sylvatica*. In the case of fruit images (a)–(c) left-hand panels represent fruit at the time of commercial harvest, and the right-hand panels, after ripening one month later. The 32-colour scale divisions indicate ranges from 0–3300 ms in (a), 0–500 ms in (b), $(0\text{–}4.5) \times 10^{-9}$ m^2 s^{-1} in (c), and −50 to 50 $\mu m\ s^{-1}$ in (d).

inserted in a 25 mm rf probe for commencement of imaging by 24 h after harvest. After completion of the various pulse sequence experiments, the rf probe containing the sample was stored at 4°C for 2 weeks, followed by 2 weeks at room temperature (18°C) to enable the fruit to reach eating ripeness. A second set of complementary measurements was subsequently collected on the same image plane of the undisturbed fruit to quantify changes during ripening.

Hedge woundwort (*Stachys sylvatica* L.) was collected from flower beds on the Massey University campus. The stems and roots of intact plants were inserted in 5 mm diameter NMR tubes with the roots immersed in water. In order to insert the stems, some root tissue was removed, how-

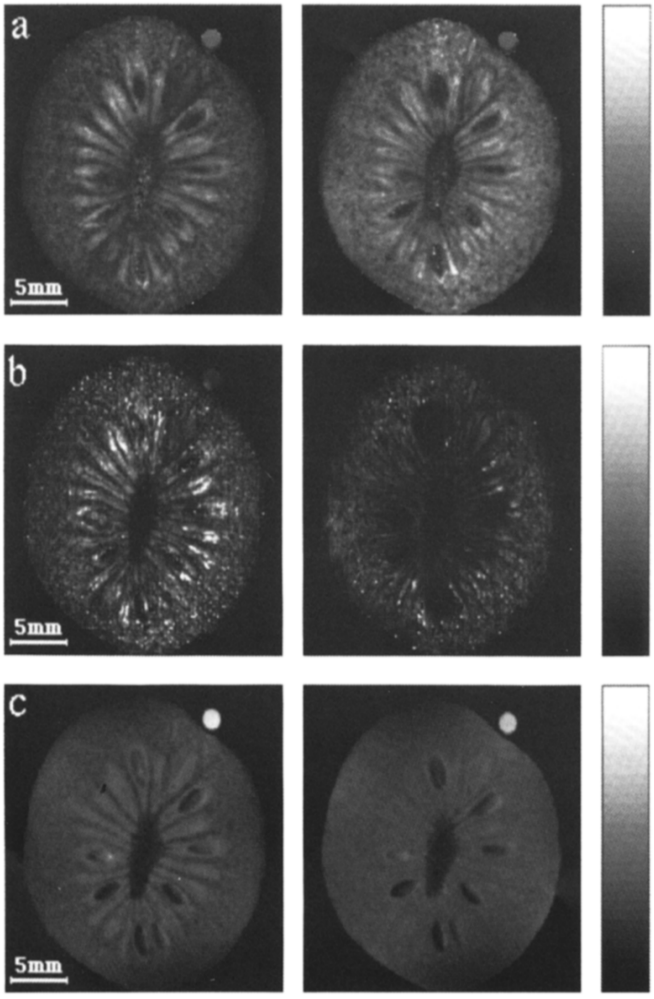

Fig. 3. Calculated relaxation maps for kiwifruit. (a) T_2-SE; (b) T_2^*; (c) T_2-CPMG proton density. Left-hand panels represent fruit at the time of commercial harvest, and the right-hand panels, after ripening one month later. The grey-scale divisions indicate range from 0–175 ms in (a) and 0–75 ms in (b) while the proton density scale is in arbitrary units.

Table 1
Relationship between maturation status, type of tissue and magnetic properties of a kiwifruit at the time of commercial harvest (soluble solids content = 6.2%) and after ripening

	T_1 (ms)	T_2-SE (ms)	T_2-CPMG (ms)	T_2^* (ms)	Diffusion [a]	% proton density [b]
fruit maturity [c]						
commercial harvest	1389	62	238	47	1850	39.4
eating ripeness	1287	83	193	32	1630	42.2
SED	13.8	2.4	4.7	4.1	7	0.5
P [d]	***	***	***	**	***	***
tissue [e] flesh						
commercial harvest	1363	51	224	41	1880	35
eating ripeness	1271	75	181	32	1660	40
locule						
commercial harvest	1439	84	266	61	1780	48
eating ripeness	1319	99	217	32	1580	47

[a] Units $\times 10^{-12}$ m^2 s^{-1}.
[b] Results expressed as percent of phantom measurement (proton density = 100%).
[c] ANOVA results based on comparison of 12 measurements of each parameter at each maturity date. The regions of interest selected at harvest were reanalysed one month later to establish changes during ripening.
[d] ** and *** represent probabilities at the < 0.01 and $< 0.001\%$ levels, respectively.
[e] Averages based on $n = 8$ measurements for flesh–each one the mean of 316 pixels, and $n = 4$ measurements for locules (but not seeds)–each the mean of 25 pixels. Full analysis of statistical differences between tissues is reserved for a subsequent publication examining changes in relaxation parameters during fruit development, as well as ripening (Clark, Callaghan and Forde, unpublished results).

ever the plants stayed turgid throughout the imaging experiments, typically lasting a period of 2 to 3 h.

3.2. Imaging

Proton NMR images were obtained using a 7.1 Tesla, 300 MHz Bruker AMX-300 NMR spectrometer. For each kiwifruit experiment, irrespective of pulse sequence, the acquisition bandwidth was 50 kHz, the slice thickness was 1 mm and the images (Figs. 2 to 4) were reconstructed on 256 × 256 pixel arrays giving an in-plane resolution of 98 μm. Corresponding parameters for *Stachys* were 40 kHz, 0.5 mm, 256 × 256 and 23 μm.

Calculated images containing quantitative data for T_1, T_2-SE, T_2-CPMG and T_2^* were reconstructed from their respective image sequences by

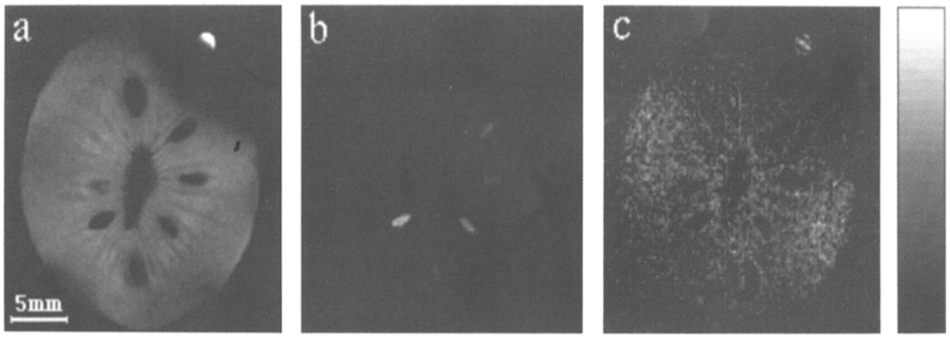

Fig. 4. Chemical shift selective images of a kiwifruit after ripening. (a) Water, (b) oil; (c) sugar images. The water image has $T_E = 17$ ms and $T_R = 2000$ ms. The oil and sugar images were both obtained with $T_E = 17$ ms and $T_R = 500$ ms.

linear regression to the semi-logarithmic data plots for each pixel. This was carried out using IMAGESHOW, a program with mapping features developed for Macintosh platforms, as described by Xia et al. [25]. Diffusion maps were calculated within the same software by the method of Stejskal and Tanner [26], while velocity maps were obtained using Fourier analysis [27]. Analysis of relaxation and velocity data (Table 1) from selected areas within an image was accomplished using the National Institute of Health program, IMAGE [28].

For T_1 relaxation time measurements, repetition times were varied between 50 and 3200 ms. For transverse relaxation measurements a repetition time of 2000 ms was used to ensure minimum T_1 weighting while delay times were as follows: for T_2-SE, T_E varied from 12 to 120 ms; for T_2^*, T_E varied from 3.6 to 20 ms; while for T_2-CPMG, the relaxation delay varied from 16.2 to 163.5 ms, with a constant pulse separation of 5 ms. In each case the relevant delay times were incremented so as to provide an approximately logarithmic spread. For measurements of diffusion and flow the PGSE gradient was incremented in 16 steps to a maximum value of 1.2 T m^{-1}. For the kiwifruit diffusion measurements the values of δ and Δ were 2 and 5 ms, respectively, whilst for the *Stachys* flow the corresponding values were 0.7 and 203 ms. In all experiments two transients were signal-averaged for each read across k space, except for the chemical shift-selective imaging where eight transients were averaged to improve signal-to-noise ratios for the less abundant molecular species.

4. Results and discussion

Fig. 2 compares T_1 relaxation, T_2-CPMG relaxation and diffusion maps for the kiwifruit at harvest and at one month after ripening. The corresponding T_2-SE and T_2^* relaxation images are shown in Fig. 3 along with the proton density image obtained by extrapolating the T_2-CPMG data back to zero delay time. All images are dominated by the water proton signal and can therefore be considered to be characteristic of the interactions and dynamics of these spins. Comparison of quantitative measurements of the phantom in each of the paired images (Figs. 2 and 3) indicated that the data were consistent within a standard deviation for each parameter investigated. This gives us some confidence in the absolute values obtained in the fruit images, without the necessity for normalization.

In each case the ripening process has apparently resulted in changes in the imaged NMR parameters. In attempting to understand these changes it is helpful to begin by comparing the diffusion maps since these relate most directly to absolute molecular properties. There is a significant reduction in diffusion coefficient (Fig. 2c) which is confirmed in the statistical analysis shown in Table 1. This is consistent with a viscosity enhancement which would arise from elevation of the sugar concentration during ripening resulting from metabolic degradation of starch granules [29]. Chemical analysis showed that the total free sugar concentration in companion fruit increased fourfold over this period from 108 to 434 mg g^{-1} dry weight, and was accompanied by a concomitant decline in starch from 337 to 23 mg g^{-1} dry weight. The remaining relaxation maps are consistent with this hypothesis. For example, both T_1 and T_2-CPMG values in the flesh and locule (tissue adjacent to the seeds) are shorter in the ripened fruit (Table 1), as would be expected if the rotational correlation times of the molecules were increased due to more frequent interaction with sugar molecules. We note that a similar reduction in relaxation times with increasing sugar content has been found in solution studies [30].

The anomalous behaviour of T_2-SE arises because of attenuation due to diffusion in the read gradient. As the water diffusion slows, upon ripening, this attenuation decreases and the consequent reduction in T_2-SE is less severe. The particular spin-echo pulse sequence used to obtain this map utilises a variable time delay between the initial dephasing read gradient pulse and the final readout, as shown in Fig. 1a. This diffusive influence in standard spin-echo estimates of T_2 values was pointed out in a recent article by Brandl et al. [31] and is entirely avoided

by applying a CPMG pulse train *before* the precursor read pulse, the method used in the T_2-CPMG sequence (Fig. 1b). Our calculations based on the known imaging parameters and measured diffusion coefficients are quite consistent with the magnitudes of T_2 reduction apparent when using the T_2-SE sequence rather than the CPMG method.

Water proton densities also show a distinct increase with ripening (Table 1). This could be due to absorption of water from the surrounding atmosphere (G.S. Smith, unpublished results), or to the release of hitherto 'invisible' bound water [32,33] from degeneration of cell wall polymer.

The T_2^* images are difficult to interpret due to a number of competing influences. One would normally expect the relaxation rate under a gradient echo to be dominated by the effect of dephasing in local fields. As expected, in each case T_2^* values were the shortest of all relaxation times measured (Table 1). A surprising feature of our work is the very short T_2^* values found in the water phantoms where local fields are expected to be minimal. This suggests that B_0 field inhomogeneity due to shimming imperfection is playing a major role in causing signal dephasing, especially near the outer regions of the image. Such effects are also likely to be present in the centre of the image, albeit to a lesser extent. Consequently, the absolute magnitudes of T_2^* values are not indicative of local structure. However, local variation in T_2^* can indicate the presence of boundaries in diamagnetic susceptibility. One of the best ways to indicate such boundaries is by means of a gradient echo image acquired using a fixed delay, a standard technique in clinical magnetic resonance imaging [24].

The data suggest that quantitative differences in NMR parameters exist between the different tissue components within the fruit (Table 1). For example, we note that the locule relaxation times were consistently longer than those in the flesh which in turn were greater than those in the seeds. Relaxation times in the core showed no consistent pattern in relation to measurements from the other three tissues. Such differences contain potentially useful information about the motion of water molecules within these regions but discussion of them is beyond the scope of this paper.

The chemical shift images resulting from selective excitation of the water, oil and sugar peaks in the NMR spectrum are shown for the ripened kiwifruit in Fig. 4. In these images some phase artifacts are apparent near the perimeter, probably due to rf inhomogeneity. Furthermore a small residual water excitation is apparent for the phantom in the sugar image of Fig. 4c. Nonetheless a clearly identified sugar peak was observed in the NMR spectrum and the majority of the signal arises from that peak. Consequently this image suggests the presence of sugar distributed evenly throughout the flesh and locules. This contrasts with the findings of Goodman et al. for grapes where the sugar distribution was non-uniform [34]. The most dramatic feature of the chemical shift selective imaging can be seen in the oil image where it is clear that the vast majority of the lipid is located in the seeds. This is consistent with the findings of other workers in chemical shift selective imaging of seeds and nuts [14,35].

To demonstrate flow contrast we have chosen to image a plant stem, *Stachys sylvatica*, in which transpiration from the leaves causes water motion upwards through the xylem. The resulting velocity map is shown in Fig. 2d along with a standard spin echo image corresponding to the water proton distribution. Flow is clearly visible in the vascular tissue toward the corners of the square cross section. The velocity is on the order of 70 $\mu m\ s^{-1}$ in the direction from roots to leaves. This velocity is close to the lower measurement limit possible using NMR [22] and is consistent with flow measurements made on the same plant at lower field strengths [36].

5. Conclusions

The NMR imaging work reported here demonstrates an unusually wide range of pulse sequences and demonstrates the potential of comparative multi-dimensional contrast in elucidating physiological processes. In the present instance we have utilised this approach to observe

fruit ripening and xylem transport. In the kiwifruit study, all parameters were sensitive to the ripening process. However, the diffusion coefficient provides the least ambiguous indication of the state of the water and therefore provides a logical starting point for any interpretation. The key to understanding the change in the diffusion coefficients was parallel information concerning the chemical state of the fruit. This indicates the importance of simultaneous physico-chemical measurements in such studies. In this context the chemical shift imaging provides useful additional insight.

One important conclusion of this work concerns the need to use precursor CPMG pulse trains in T_2 mapping, rather than the conventional spin echo sequence of Fig. 1a. While the spin echo works well for T_2 mapping in large scale (e.g. medical) imaging, in high-resolution studies, where the distance diffused by the molecules over the echo time T_E becomes comparable with the pixel dimension, this sequence can lead to strong diffusive attenuation effects. The CPMG sequence shown in Fig. 1c avoids such problems.

Many prior imaging studies on plants have emphasised the usefulness of spin echo and gradient echo images in accentuating anatomical features. We have shown here that by extending the range of pulses sequences employed, it is possible to reveal dynamical features associated with molecular motion.

Acknowledgements

This work was supported by funding from the New Zealand Lotteries Grants Board and the New Zealand Foundation for Research, Science and Technology.

References

[1] G. Gassner, in: Nuclear magnetic resonance in agriculture, eds. P.E. Pfeffer and W.V. Gerasimowicz (CRC Press, Boca Raton, USA) pp. 405–428.
[2] P.J. Kramer, J.N. Siedow and J.S. MacFall, in: Measurement techniques in plant science, eds. Y. Hashimoto, P.J. Kramer, H. Nonami and B.R. Strain (Academic Press, New York, 1990) pp. 403–431.
[3] G.A. Johnson, L.W. Hedlund, G.P. Cofer and S.A. Sudarth, Rev. Magn. Reson. Med. 4 (1992) 187–219.
[4] V. Sarafis, J. Pope and Y. Sarig, in: Magnetic resonance microscopy: methods and application in materials science, agriculture and biomedicine, eds. B. Blümich and W. Kuhn (VCH, New York, 1992) pp. 459–476.
[5] S.Y. Wang, P.C. Wang and M. Faust, Sci. Hortic. 35 (1988) 227–234.
[6] P. Chen, M.J. McCarthy and R. Kauten, Trans. ASAE 32 (1989) 1747–1753.
[7] N. Ishida, T. Kobayashi, M. Koizumi and H. Kano, Agric. Biol. Chem. 53 (1989) 2363–2367.
[8] C.Y. Wang and P.C. Wang, Hortic. Sci. 24 (1989) 106–109.
[9] J.C. Pech, A. Latche, M.H. Andrieu and J. Pradere, Abstr. XXIII Intern. Hortic. Congress 1 (1990) 635.
[10] B.A. Goodman, B. Williamson and J.A. Chudek, Protoplasma 166 (1992) 107–109.
[11] B.A. Goodman, B. Williamson and J.A. Chudek, New Phytol. 122 (1992) 529–535.
[12] S.L. Duce, T.A. Carpenter and L.D. Hall, J. Food Eng. 16 (1992) 165–172.
[13] J.L. Maas, M.J. Line, M.M. Millard and G.J. Galletta, Advan. Strawberry Res. 11 (1992) 64–66.
[14] J.M. Pope, in: Magnetic resonance microscopy: methods and application in materials science, agriculture and biomedicine, eds. B. Blümich and W. Kuhn (VCH, New York, 1992) pp. 441–457.
[15] C.Y. Wang and P.C. Wang, Environ. Exp. Bot. 32 (1992) 213–219.
[16] B. Williamson, B.A. Goodman and J.A. Chudek, New Phytol. 120 (1992) 21–28.
[17] P. Chen, M.J. McCarthy, R. Kauten, Y. Sarig and S. Han, J. Agric. Eng. Res. 55 (1993) 177–187.
[18] B.A. Goodman, B. Williamson, J.A. Chudek, Magn. Reson. Imag. 11 (1993) 1039–1041.
[19] B. Williamson, B.A. Goodman and J.A. Chudek, Micron 24 (1993) 377–383.
[20] S.L. Duce, T.A. Carpenter, L.D. Hall and B.P. Hills, Magn. Reson. Imag. 10 (1992) 289–297.
[21] J.R. MacFall, F.W. Wehrli, R.K. Greger and G.A. Johnson, Magn. Reson. Imag. 5 (1987) 209–220.
[22] P.T. Callaghan, Principles of nuclear magnetic resonance microscopy (Oxford Univ. Press, Oxford, 1991).
[23] P.T. Callaghan and Y. Xia, J. Magn. Reson. 91 (1991) 326–352.
[24] P. Mansfield and P.G. Morris, NMR imaging in biomedicine (Academic Press, New York, 1982).
[25] Y. Xia, A. Coy and P.T. Callaghan, IMAGESHOW® 5.0: An image processing and display software for the Macintosh™ computers, NMR Research Laboratory, Department of Physics and Biophysics, Massey University, New Zealand (1992).
[26] E.O. Stejskal and J.E. Tanner, J. Chem. Phys. 42 (1965) 288–292.

[27] P.T. Callaghan, C.D. Eccles and Y. Xia, J. Phys. E 21 (1988) 820–822.
[28] W. Rasban, NIH IMAGE 1.47: Public domain image processing and analysis program for the Macintosh™, National Institute of Health, Bethesda, USA (1992).
[29] E.A. MacRae, J.H. Bowen and M.G.H. Stec, J. Sci. Food Agric. 47 (1989) 401–416.
[30] G.G. Birch and R. Karim, J. Sci. Food Agric. 58 (1992) 563–568.
[31] M. Brandl, A. Link and A. Haase, Abstr. II Intern. Conf. Magn. Reson. Microscopy, Heidelberg (1993) 64.
[32] W. Derbyshire, Nucl. Magn. Reson. 5 (1976) 264–291.
[33] W. Derbyshire, Nucl. Magn. Reson. 7 (1978) 193–225.
[34] B.A. Goodman, B. Williamson and J.A. Chudek, Magn. Reson. Imaging 11 (1993) 1039–1041.
[35] M.R. Lakshminarayana, S. Joshi, G.A. Nagana Gowda and C.L. Khetrapal, J. Biosci. 17 (1992) 87–93.
[36] Y. Xia, V. Sarafis, E.O. Campbell and P.T. Callaghan, Protoplasma 173 (1993) 170–176.